







Article

Self-Assembly of the Bio-Surfactant Aescin in Solution: A Small-Angle X-ray Scattering and Fluorescence Study

Carina Dargel ^{1,†} , Ramsia Geisler ^{1,†} , Yvonne Hannappel ¹ , Isabell Kemker ² ,
Norbert Sewald ²  and Thomas Hellweg ^{1,*} 

¹ Physical and Biophysical Chemistry, Bielefeld University, 33615 Bielefeld, Germany; carina.dargel@uni-bielefeld.de (C.D.); ramsia.geisler@gmail.com (R.G.); yvonne.hannappel@uni-bielefeld.de (Y.H.)

² Organic and Bioorganic Chemistry, Bielefeld University, 33615 Bielefeld, Germany; isabell.kemker@uni-bielefeld.de (I.K.); norbert.sewald@uni-bielefeld.de (N.S.)

* Correspondence: thomas.hellweg@uni-bielefeld.de; Tel.: +49-0521-106-2055

† These authors contributed equally to this work.

Received: 22 February 2019; Accepted: 17 April 2019; Published: 25 April 2019



Abstract: This work investigates the temperature-dependent micelle formation as well as the micellar structure of the saponin aescin. The critical micelle concentration (*cmc*) of aescin is determined from the concentration-dependent autofluorescence (AF) of aescin. Values between $cmc_{aescin,AF}(10\text{ }^{\circ}\text{C}) = 0.38 \pm 0.09\text{ mM}$ and $cmc_{aescin,AF}(50\text{ }^{\circ}\text{C}) = 0.32 \pm 0.13\text{ mM}$ were obtained. The significance of this method is verified by tensiometry measurements. The value determined from this method is within the experimental error identical with values obtained from autofluorescence ($cmc_{aescin,T(WP)}(23\text{ }^{\circ}\text{C}) = 0.33 \pm 0.02\text{ mM}$). The structure of the aescin micelles was investigated by small-angle X-ray scattering (SAXS) at 10 and 40 °C. At low temperature, the aescin micelles are rod-like, whereas at high temperature the structure is ellipsoidal. The radii of gyration were determined to $\approx 31\text{ Å}$ (rods) and $\approx 21\text{ Å}$ (ellipsoid). The rod-like shape of the aescin micelles at low temperature was confirmed by transmission electron microscopy (TEM). All investigations were performed at a constant pH of 7.4, because the acidic aescin has the ability to lower the pH value in aqueous solution.

Keywords: saponin; aescin; critical micelle concentration (*cmc*); autofluorescence; small-angle X-ray scattering (SAXS); transmission electron microscopy (TEM); micelle structure

1. Introduction

Saponins are a class of naturally occurring bio-surfactants which share the same basic structure. On the one hand, the amphiphilic character results from the hydrophobic nature of the aglyconic part which is either constituted of a triterpene or a steroid [1–3]. On the other hand, glycosidic bonds link the aglycone to the hydrophilic, glyconic parts of the molecule which are constituted of up to three separate chains of sugars. The number of sugar chains categorizes the saponins into monodesmosides (one chain), bidesmosides (two chains, most common case), or tridesmosides (three chains, the rarest case) [4]. The high variability in the type of sugar as well as the number of these chains leads to a high diversity of saponins [5,6].

As natural surfactants, saponins are present in many common plants such as potatoes, beans, soy, and ginseng [6–8]. Consequently, saponins are supplied to the human body during ingestion, and depending on the dose, have different effects on the body. Amongst others, they have an anti-inflammatory effect [9,10] and show anti-fungal, anti-bacterial, and anti-yeast activity [7,11]. Moreover, saponins can be cytotoxic to cancer cells, but also to endogenous cells, whereby this action

might be caused by alternation of the membrane permeability [1,2,12,13]. As a result of the diverse effects of saponins, they are used in different pharmaceuticals. In addition, saponins have applications in the cosmetic, food, and agriculture sectors due to their ability to stabilize emulsions, and to solubilize bulky hydrophobic molecules [3].

The effects of saponins, which are used in a variety of ways, are all based on their amphiphilic structure. This structure allows saponins, on the one hand, to interact with biological and artificial membranes [14–16] and on the other hand to self-assemble in solution [15,17]. The micelle formation of specific saponins was examined by different groups in terms of the critical micelle concentration (*cmc*) [4,18,19] and shape of the micelles [20–24]. It was found that many saponins tend to build spherical micelles. The saponins *Rb*₁ and *Rg*₁ from ginseng form spherical micelles with diameters of up to 800 Å [25]. In comparison, the spherical micelles formed by *Quil A* with a diameter of 60 Å are very small [20]. Besides spherical micelles, elongated structures were also found for different saponins [23,26]. For the saponin *Quil A* for example, the presence of low amounts of cholesterol induces the formation of worm-like structures [24]. In addition, the pure saponin *QS-21* forms not perfectly spherical, but elongated micelles with a maximum diameter of 75 Å [22]. For the saponin glycyrrhizin, different structures are reported. In water, spherical micelles with diameters of 60–120 Å were found [27,28]. In buffer solution with a distinct pH of 6, rod-like micelles with a cross-sectional radius of 13 Å and a length of 180 Å were present [21]. The example of glycyrrhizin clearly illustrates the importance of controlled environmental conditions in the study of micelle formation, because many saponins strongly change the pH value when dissolved in water due to the acidic sugar groups attached.

In this study, the saponin *aescin* was investigated under well-defined conditions and temperatures. The monodesmosidic saponin aescin can be extracted from the seeds of the horse chestnut tree *Aesculus hippocastanum* (*Hippocastanaceae*) and is a natural mixture of triterpenic saponins [9,29,30]. Thereby, aescin exists in an α - and a β -form, both of which include molecules with slightly different structures. Both forms can be distinguished by the solubility in water and the hemolytic index. Different molecular structures of β -aescin, which is the main compound in this study, are shown in Figure 1. The aglycone is a derivative of protoaescigenin which is acylated by acetic acid at C-22 in the case of β -aescin. To the C-21 position, either an angelic or tiglic acid residue is bound [9,31–34]. These substituents and two other oxygen-containing moieties give the triterpene a polar and an apolar side. The hydrophilic, glyconic part of aescin is attached at the C-3 position via a D-glucuronic acid (GlcA). To this linker, two D-glucose (Glc) molecules are attached. One of these can be substituted by D-xylose (Xyl) [31,35,36]. Aescins α - and β -form can be converted into each other by a heat-induced acyclic migration of the residues at the positions C₂₁, C₂₂, and C₂₈ [9].

The β -form of aescin is the active component in the natural extract and is conventionally used in the treatment of chronic venous insufficiency (CVI) [9,31,34,37]. The use of aescin in this case is based on a large number of mechanisms of action. Among others, the presence of aescin in case of a hypoxia prevents the decrease in ATP concentration, which counteracts a degradation of the endothelial cells in the veins. This indirectly reduces the vein permeability [9,38].

Effects directly related to the interaction of aescin with the membranes of the cells contained in the veins have not been mentioned in this context so far. Nevertheless, it is known that aescin interacts with lipid membranes [18,39–41], but the physico-chemical interaction on the molecular scale is still not fully understood. However, the behavior of aescin in solution, especially above the *cmc*, is essential to elucidate the structure–activity relationship with lipid membranes and the mechanism of action of aescin.

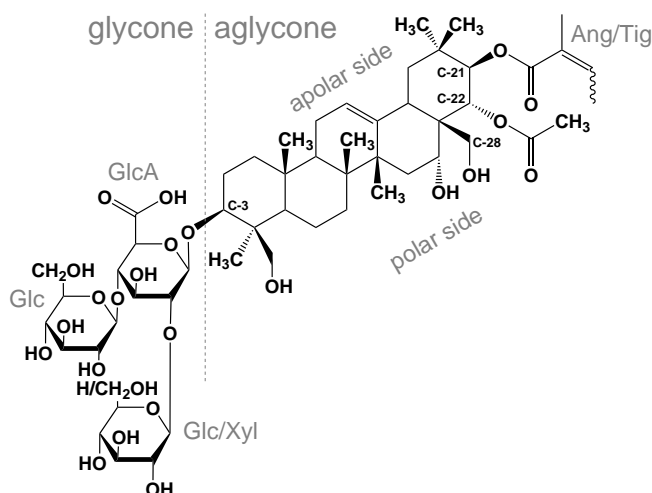


Figure 1. Molecular structure of β -aescin [31,41]. Aescin consists of a well-separated polar glyconic part constituted of three sugar molecules and a triterpene backbone, which represents the aglyconic part. Polar groups are attached to its backbone one-sided so that the aglycone possesses a slightly polar and an apolar side.

There are some reports by other groups about the *cmc* of aescin. The values reported range from ≈ 0.057 mM (equal to 0.065 mg/mL) [42], 0.088 mM [18] and ≈ 0.1 mM [43] to 0.78 mM [44]. These values were obtained by tensiometry experiments in aqueous solution at temperatures between 20 and 30 °C and at different pH values. Thereby, Penfold et al. [43] investigated a pH range from 4 to 8 and a significant change of the *cmc* was not found. The size and shape of aescin micelles in water with unspecified pH was first reported by de Groot et al. [42] By transmission electron microscopy (TEM), they indicate the presence of micelles with circularly shaped 2D projection exhibiting an average diameter of 200 Å coexisting with ellipsoidal objects with a similar average length of 200 Å.

In this work, we determine the *cmc* of aescin in aqueous phosphate buffer solution at a physiological and constant pH of 7.4. As a result of the D-glucuronic acid present in the glyconic part of aescin, the pH value decreases when aescin is dissolved in water. Another factor which may influence the *cmc* of aescin is the temperature of the solution. As a consequence of the temperature-dependent solubility of surfactant molecules in aqueous solution, the overall size and shape of the micelles may change. The measurement technique employed to determine the *cmc* in a temperature-dependent manner was fluorescence spectroscopy, whereby the concentration-dependent autofluorescence of aescin was detected. Results obtained by this method were verified by tensiometry. The temperature- and concentration-dependent structure of the micelles was investigated by transmission electron microscopy (TEM) and small-angle X-ray scattering (SAXS). SAXS provides in-situ structural information and is less prone to artifacts compared to TEM.

2. Experimental

2.1. Materials and Sample Preparation

The saponin aescin ($\geq 95\%$, CAS number 6805-41-0) was purchased from Sigma Aldrich (Munich, Germany). The composition of the aescin powder was determined by (analytical) reversed-phase high pressure liquid chromatography (RP-HPLC) followed by mass spectrometry as well as ^1H -NMR spectroscopy. A detailed description of the fractionation can be found in the Supplementary Materials. Two separable fractions were obtained by RP-HPLC (Figure S1), which show very similar mass spectra (Figure S2). Both fractions exhibit the same exact mass of 1130.5 g/mol and similar fragmentation patterns. This indicates the presence of isomers. Analysis of the ^1H -NMR spectra (Figure S3/S4, Table S1) revealed the presence of cis-trans-isomers of β -aescin with either tiglic (fraction 1) or angelic acid (fraction 2) bound to C-21 and an acetic group bound to C-22. Proton signal assignment was

done on the basis of works of Yoshikawa et al. [45,46] and the presence of three sugar moieties was verified. As a result of the numerous protons in the sugar residues, the presence of D-xylose instead of D-glucose could not be detected.

Experiments in this study were performed with the non-purified β -aescin. Because dissolving aescin in water decreases the pH value drastically and the solubility in water is bad, samples were prepared in a 50 mM phosphate buffer with a constant pH value of 7.4. For the preparation of the buffer deionized, purified water (Sartorius arium VF pro, Göttingen, Germany) was used. A stock solution of aescin in the highest concentration was prepared and the pH value of this solution was also adjusted to pH 7.4. All other aescin solutions were prepared by dilution with buffer.

2.2. Fluorescence Spectroscopy

Fluorescence spectroscopy was used to determine the *cmc* of aescin. The experiments were performed on a Jasco FP-8300 fluorescence spectrometer (JASCO, Pfungstadt, Germany). Therefore, the samples were excited at a wavelength of 370 nm and the emission recorded in a wavelength range between 400 nm and 800 nm. The excitation as well as the emission bandwidth were 5 nm and the response time was set to 0.2 s. The samples were measured in a fluorescence cuvette with a light path of 10 mm (Hellma Analytics, Müllheim, Germany). The temperature-dependent autofluorescence of aescin was recorded for several aescin concentrations in a temperature range between 10 and 50 °C in steps of 5 °C. The equilibration time between two different temperatures was at least five minutes.

2.3. Tensiometry

To determine the *cmc*-value of aescin by tensiometry experiments, the Wilhelmy plate as well as the Du Noüy ring method were used. Measurements were done at a temperature of 23 °C with a DCAT 21 tensiometer from dataphysics (Filderstadt, Germany) using a platinum-iridium-plate/ring. The plate/ring was cleaned before each measurement by heating on a flame and rinsing with buffer solution. The phosphate buffer was taken as initial phase and a concentrated aescin solution was added step-wise. The surface tension was measured after stirring and an equilibration time of five minutes.

2.4. Transmission Electron Microscopy

TEM images were taken with a JEOL JEM-2200FS electron microscope (JEOL, Freising, Germany) equipped with a cold field-emission electron gun. The microscope was operated at an acceleration voltage of 200 kV. All images were recorded digitally by a bottom-mounted camera (Gatan OneView, Gatan, Pleasanton, CA, USA) and processed with a digital imaging processing system (Digital Micrograph GMS 3, Gatan, Pleasanton, CA, USA).

The samples (3 μ L) were placed on TEM carbon coated copper grids (ECF200-Cu, 200 mesh, Science Services, Munich, Germany) at a temperature of 6 °C. After 1 min, the residual water was blotted off with a filter paper. Then, the samples were stained with 3 μ L of uranyl acetate (2 wt% aqueous solution) for 1 min and dried again with filter paper. To achieve good statistics several positions on each grid were imaged.

2.5. Small-Angle X-ray Scattering

SAXS measurements on specific aescin solutions were performed on an in-house SAXS/WAXS system (XEUSS, Xenocs, Sassenage, France) at temperatures of 10 and 40 °C. The instrument was equipped with a CuK_α source ($\lambda = 1.541 \text{ \AA}$, GeniX ultra low divergence, Xenocs) and a Pilatus 300K hybrid pixel detector (Dectris, Baden Deattwil, Switzerland). The samples were measured at a sample-to-detector distance of 820 mm, which yields a q -range of $0.05\text{--}0.3 \text{ \AA}^{-1}$. For the measurement, a flow-through Kapton capillary (1 mm inner diameter, Good-Fellow GmbH, Bad Nauheim, Germany) positioned in a Linkam stage (Linkam Scientific, Tadworth, UK) was used. The scattering intensity of the sample was normalized by taking into account the sample thickness, the acquisition time, the transmission, and the background scattering signal of the setup. For normalization to the incident

intensity, glassy carbon type 2 [47] as standard was used. The data acquisition time was several hours per temperature and sample. The 2D data were reduced with the Foxtrot software [48].

The scattering intensity can be described by the general equation: $I(q) = N \cdot (\Delta\rho)^2 \cdot V \cdot P(q) \cdot S(q)$. Other than the number of particles N , it depends on the scattering volume V , the contrast between solvent and particle $\Delta\rho = \rho_{\text{particle}} - \rho_{\text{solvent}}$, the form factor $P(q)$, and the structure factor $S(q)$. The scattering vector magnitude is $q = \frac{4\pi}{\lambda} \sin(\theta)$ with θ being half the scattering angle.

3. Results

3.1. Determination of the Critical Micelle Concentration of Aescin

3.1.1. Determination of $cmc_{\text{aescin,AF}}$ by Fluorescence Spectroscopy

The aim of this work is to determine the cmc value of aescin under well-defined conditions (pH and temperature). At pH 7.4, aescin is deprotonated at its glucuronic acid group and nicely dissolves in aqueous buffer. The pK_a -value of aescin in water was determined by titration to a value of 4.7 ± 0.2 (see Figure S5). One established method to determine cmc -values is fluorescence spectroscopy. Thereby, often external fluorophores such as ammonium 8-anilino-1-naphthalenesulfonate (ANS) or pyrene are added [49–51]. The cmc in these cases is derived from the surfactant concentration-dependent intensity and/or shape change of the fluorophores fluorescence spectra resulting from the incorporation of the fluorophore into the surfactant micelles [49]. An influence of added fluorophores on the micellation process of the surfactant cannot be fully excluded in the most cases.

To avoid an outer influence on the cmc results, the cmc is determined from the autofluorescence of aescin itself without any additive in this work. An analogous principle was used by Balakrishnan et al. to determine the cmc of the *Sapindus* saponin [19]. Fluorescence measurements were performed in a temperature range of 10 and 50 °C. The recorded autofluorescence spectra of aescin solutions upon excitation at 370 nm at different concentrations at a temperature of 20 °C are shown in Figure S6. Figure 2 displays the concentration normalized intensity evolution of the autofluorescence maximum ($\lambda_{\text{max}} = 450 \text{ nm}$) as function of aescin concentration for temperatures of 10, 30, and 50 °C. For this, the autofluorescence intensity was divided by the respective aescin concentration. With that, $I_{\text{aescin,450nm}} \cdot c_{\text{aescin}}^{-1}$ expresses the autofluorescence ability of an ensemble of a defined number of aescin molecules. $I_{\text{aescin,450nm}} \cdot c_{\text{aescin}}^{-1}$ decreases with increasing temperature and strongly reduces upon micelle formation. The concentration-dependent behavior is not modified significantly by temperature variation.

The intersection of the two linear regressions in Figure 2 defines the value of $cmc_{\text{aescin,AF}}$. Table 1 lists the temperature-dependent $cmc_{\text{aescin,AF}}$ values. For the linear regression at concentrations below $cmc_{\text{aescin,AF}}$, the first six concentrations were taken into account. In contrast, the last five points were fitted for the linear regression at concentrations above $cmc_{\text{aescin,AF}}$. Values in the $cmc_{\text{aescin,AF}}$ region were not considered for fitting. The regressions were extrapolated to illustrate the intersection point. The error of the $cmc_{\text{aescin,AF}}$ values was calculated by error propagation from the errors of the linear regressions and results herewith from the statistics of the measured data. $cmc_{\text{aescin,AF}}$ values between $0.38 \pm 0.09 \text{ mM}$ (at 10 °C) and $0.32 \pm 0.13 \text{ mM}$ (at 50 °C) were obtained. Hence, within the experimental precision, $cmc_{\text{aescin,AF}}$ does not depend on temperature. Comparison with cmc_{aescin} values from other groups shows that the values received in this study are in the range of values determined before under slightly different conditions [18,42–44]. It should not be neglected that different *aescins* might show different cmc_{aescin} values due to varied compositions of the single components. To verify the method of cmc_{aescin} determination from autofluorescence, additional tensiometry experiments were performed (see Section 3.1.2).

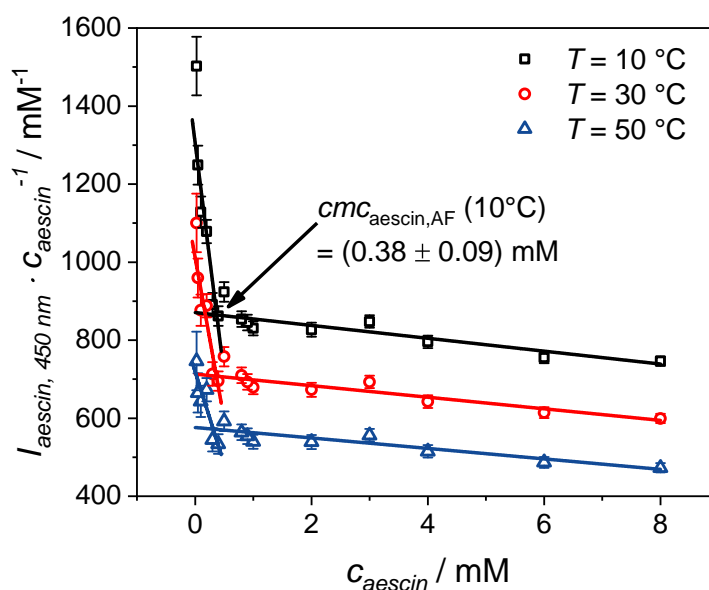


Figure 2. Autofluorescence intensity of aescin normalized with respect to each aescin concentration ($I_{\text{aescin}, 450 \text{ nm}} \cdot c_{\text{aescin}}^{-1}$) as a function of aescin concentration c_{aescin} at temperatures of 10, 30, and 50 °C. The intersection of the two regressions defines the value of $cmc_{\text{aescin}, \text{AF}}$ for each temperature.

Table 1. Temperature-dependent $cmc_{\text{aescin}, \text{AF}}$ values determined from aescins autofluorescence intensity (see Figure 2).

T °C	$cmc_{\text{aescin}, \text{AF}}$ mM
10	0.38 ± 0.09
15	0.38 ± 0.10
20	0.38 ± 0.10
25	0.38 ± 0.10
30	0.37 ± 0.11
35	0.37 ± 0.12
40	0.35 ± 0.13
45	0.35 ± 0.14
50	0.32 ± 0.13

The strong decrease in the autofluorescence intensity indicates the presence of quenching effects, as seen for aescin in Figure 2. This might be due to a very specific arrangement of the aescin molecules inside the micelles. Molecular dynamics (MD) simulations by Tsibranska et al. [52] for the self-assembly of aescin molecules at the water–air interface confirmed multiple attractive interactions between its hydrophobic and hydrophilic parts. Moreover, Penfold et al. [43] proved this directed self-assembly experimentally by neutron reflectivity. Hence, we expect a directed self-assembly with a defined arrangement of aescin molecules inside the micelles. Here, hydrophobic interactions between the triterpenes and/or hydrogen bonds between the sugar groups could lead to the observed strong fluorescence quenching.

3.1.2. Determination of $cmc_{\text{aescin}, T}$ by Tensiometry

Tensiometry is the most commonly used method to determine critical micelle concentrations. In this study, this method was used to verify the results obtained from the autofluorescence measurements of aescin. Figure 3 shows the obtained surface tension (SFT) as function of the aescin concentration using the Wilhelmy plate (WP) method at a temperature of 23 °C. Data measured with the Du Noüy ring (DNR) method are additionally shown in Figure S7.

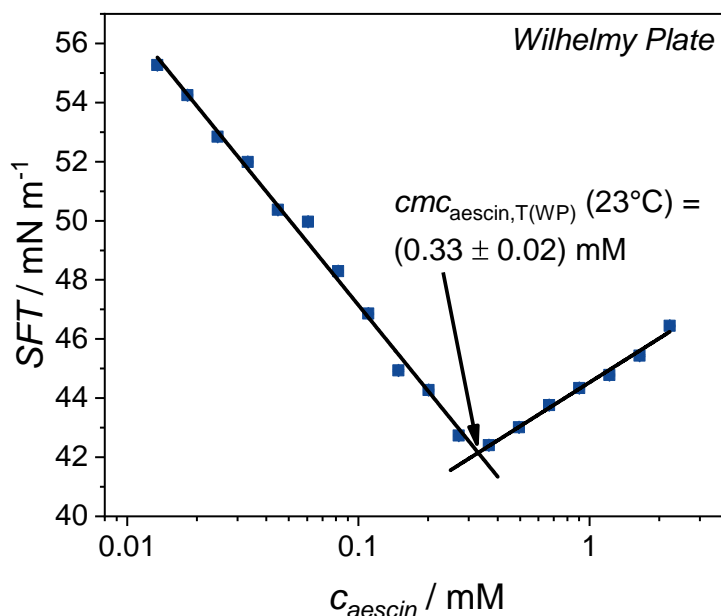


Figure 3. Surface tension isotherm of aescin in aqueous phosphate buffer at a temperature of 23 °C recorded with the Wilhelmy Plate (WP) method. The intersection of the two linear regressions defines the $cmc_{aescin,T(WP)}$ value. The increase in surface tension (SFT) above $cmc_{aescin,T(WP)}$ might result from impurities of the aescin powder [53–55].

Below $cmc_{aescin,T(WP)}$ SFT decreases with increasing c_{aescin} due to the assembly of aescin molecules on the buffer–air interface. The point of minimal SFT and hence, the saturation of the interface with aescin molecules defines the critical micelle concentration. The $cmc_{aescin,T(WP)}$ -value of 0.33 ± 0.02 mM for a temperature of 23 °C was determined from the intersection of the two linear regressions applied to the regions below and above $cmc_{aescin,T(WP)}$. The given error originates from error propagation. By using the Du Noüy ring method, within the experimental error, an identical value of $cmc_{aescin,T(DNR)} = 0.30 \pm 0.06$ mM was received (see Figure S7). Hence, within the experimental precision, the values obtained here equal the $cmc_{aescin,AF}$ values determined by autofluorescence at similar temperature. This verifies the validity of the autofluorescence method.

Above $cmc_{aescin,T(WP)}$ a reproducible increase of SFT is visible. A similar behavior was also observed for different surfactants like sodium dodecyl sulfate (SDS) and cationic lysosomotropic substances [53–55]. In all cases, the increase in the surface tension above the cmc was assigned to impurities of the surfactants, whereby a substance with a higher surface activity compared to the surfactant investigated might be present [55]. Because the aescin powder used in this study has a purity of 95 %, presence of impurities is possible. When dissolved in seawater, an increase in SFT above $cmc_{aescin,T}$ was also reported for aescin by Pekdemir et al. [44].

Moreover, time-dependent measurements of the SFT at a constant aescin concentration indicated that not having reached an equilibrium state can be presumably excluded as reason for the increase of SFT at concentrations above cmc_{aescin} (see Figure S8). The SFT does not change significantly over time in comparison to the last value obtained from the titration experiment. Stanimirova et al. investigated the kinetics of the long-term adsorption of a *Quillaja* saponin by tensiometry [56]. They found two characteristic time constants of ≈ 30 s and ≈ 250 s for the adsorption of the saponin at the surface at a concentration above the cmc [56]. If a similar behavior is assumed for aescin, comparison of these values with the minimum time of ≈ 420 s between two surface tension measurements (including time for equilibration and measurement) supports the hypothesis that, most likely, impurities are responsible for the increase in SFT rather than not having reached an equilibrium state.

3.2. Structural Investigation of Aescin Micelles

In order to investigate the shape of the micellar structures, aqueous suspensions containing aescin at different concentrations well above the *cmc* (1.7 to 9.5 mM) were analyzed by TEM and SAXS. The SAXS measurements were performed at two different temperatures in order to prove whether the shape of the aescin micelles is dependent on temperature or not.

3.2.1. TEM—Aescin Micelle Structure at Low Temperature

TEM images were recorded of exemplary samples with aescin concentrations of 2.5 and 5.5 mM (Figure 4). Preparation of the TEM sample was done at a temperature of 6 °C.

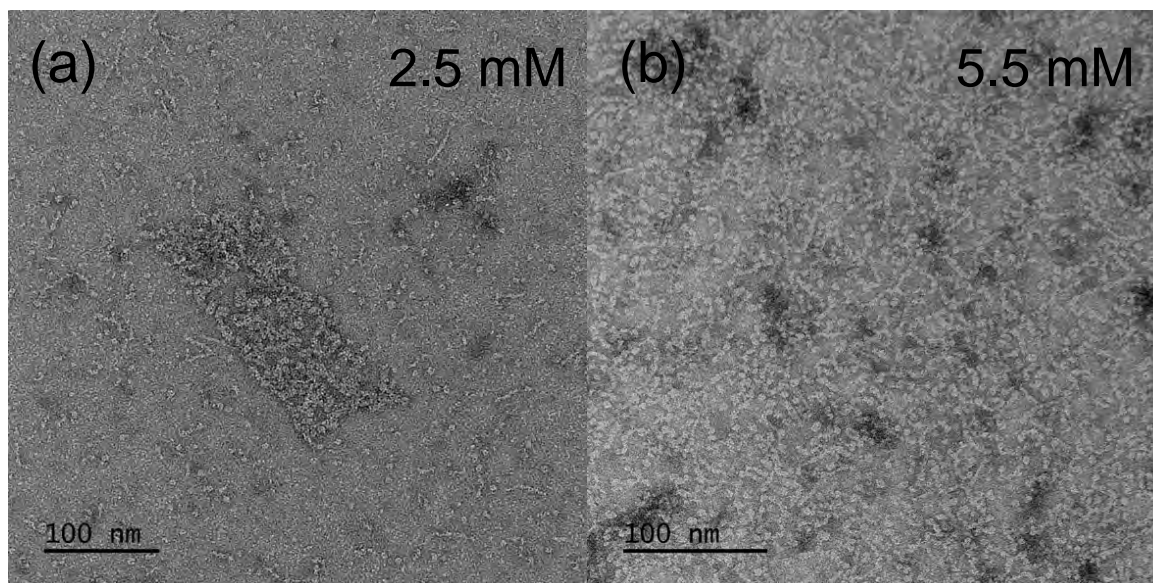


Figure 4. Transmission electron microscopy (TEM) images of aescin solutions with concentrations of (a) 2.5 mM and (b) 5.5 mM. The samples were deposited on TEM grids, stained and dried at 6 °C.

The samples exhibit a micellar structure at both concentrations. The micelles found have rod-like shape and are accompanied by smaller, rather spherical objects. Moreover, it seems very likely that these smaller objects assemble into elongated rods, especially because the number of the spherical objects is much smaller for the sample with the higher aescin concentration. The size of the rod-like micelles is roughly 25–35 Å for cross-sectional diameter (D) and 70–150 Å for the length (L). This equals an average radius of gyration R_G of 33 ± 11 Å, when using the relation $R_G = \sqrt{\frac{(0.5 \cdot D)^2}{2} + \frac{L^2}{12}}$ for cylindrical objects with $D = 30 \pm 5$ Å and $L = 100 \pm 40$ Å.

3.2.2. SAXS—Shape of Aescin Micelles

Small-angle X-ray scattering experiments were performed at 10 and 40 °C. The data were analyzed by the standard indirect Fourier transform (IFT) method in the GIFT software package by O. Glatter [57]. The data at 10 °C were approximated with a set of non-equidistant splines covering a shorter and a longer length scale of the object analyzed. The data at 40 °C were approximated by only one length contribution. On the r -scale, the data were approximated with 10 non-equidistant points per spline for both temperatures. The cutoffs of the IFT fits at high q were made to guarantee stable fit results. In consequence, probable deviations of the resulting $p(r)$ functions at low r can be considered as erroneous and negligible. The fits resulting from the IFT analysis are shown in Figure 5. The corresponding $p(r)$ functions are shown in Figure 6a,b for 10 and 40 °C, respectively.

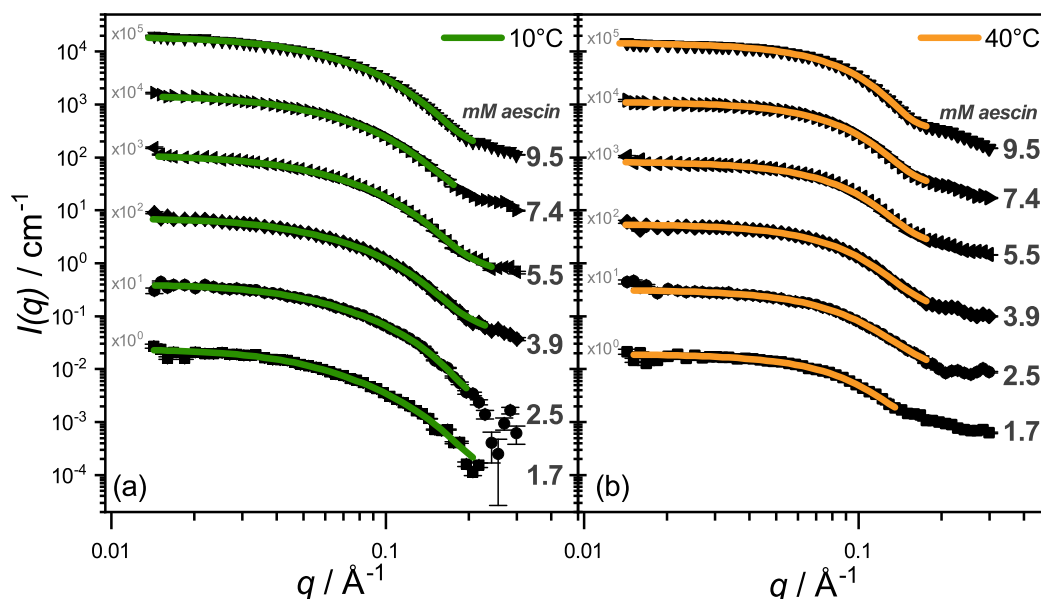


Figure 5. Fits by indirect Fourier transformation (IFT) analysis to small-angle X-ray scattering (SAXS) data of aescin solutions with different concentrations at temperatures of (a) 10 and (b) 40 °C [57]. The data are scaled by the factors given in gray.

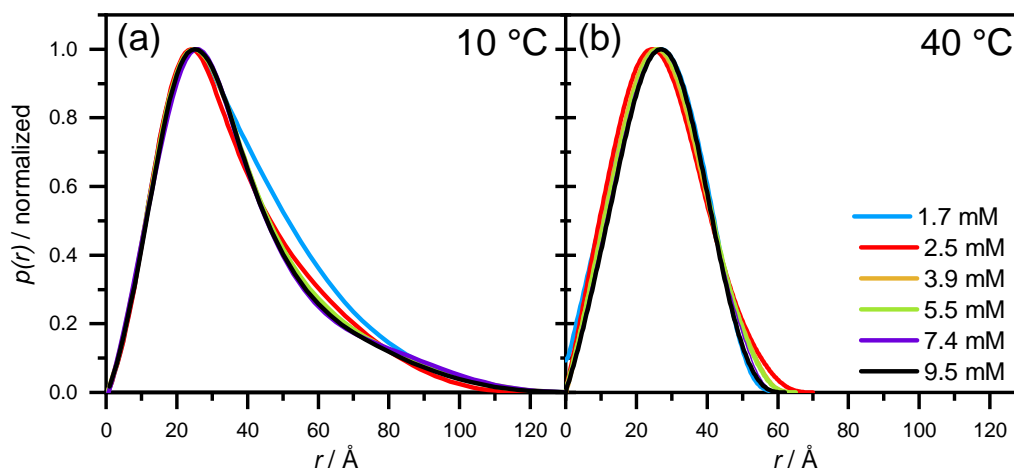


Figure 6. Pair distance distribution functions ($p(r)$) of aescin containing aqueous solutions at (a) 10 °C and (b) 40 °C for different aescin contents. The scattering data were analyzed with the standard IFT method [57].

At 10 °C, $p(r)$ functions indicate that the micelles formed have an elongated shape which extends to roughly 120 \AA for all concentrations measured. At 40 °C, structures exhibit a rather symmetrical shape which can be either spherical or ellipsoidal. Here, maximum dimensions reach 60–70 \AA . The overall shape and size of the samples does not vary significantly with aescin concentration. R_G values are obtained through integration of the $p(r)$ function (Equation (1)).

$$R_G^2 = \frac{\int p(r)r^2 dr}{2 \int p(r) dr}. \quad (1)$$

Similar values were obtained for all aescin concentrations at the same temperatures. At 10 °C a value of $R_G(10^\circ\text{C}) = 30.8 \pm 0.6 \text{ \AA}$ and at 40 °C a value of $R_G(40^\circ\text{C}) = 21.2 \pm 0.4 \text{ \AA}$ was obtained. The value at low temperature (10 °C) nicely corresponds to the R_G -value calculated from the particle dimensions

determined by TEM. Hence, when increasing the temperature, the rod-like arrangement is distorted and the particles appear less elongated.

3.2.3. SAXS: Model-Dependent Fitting of Aescin Micelles

To gain more precise information about the structural parameters of the micelles, analytical form factor model functions were also fitted to the SAXS data. The best agreement with the scattering data was achieved when fitting the curves at 10 °C with a *cylinder* model ($V_{\text{cylinder}} = \pi R^2 L$) and with an *ellipsoid* model ($V_{\text{ellipsoid}} = \frac{4}{3} \pi R_p R_e^2$) at 40 °C. Equations describing these models can be found in the SasView documentation [58]. The SAXS curves for the samples with different aescin contents at both temperatures are shown together with the model fits in Figure 7a,b for 10 and 40 °C, respectively.

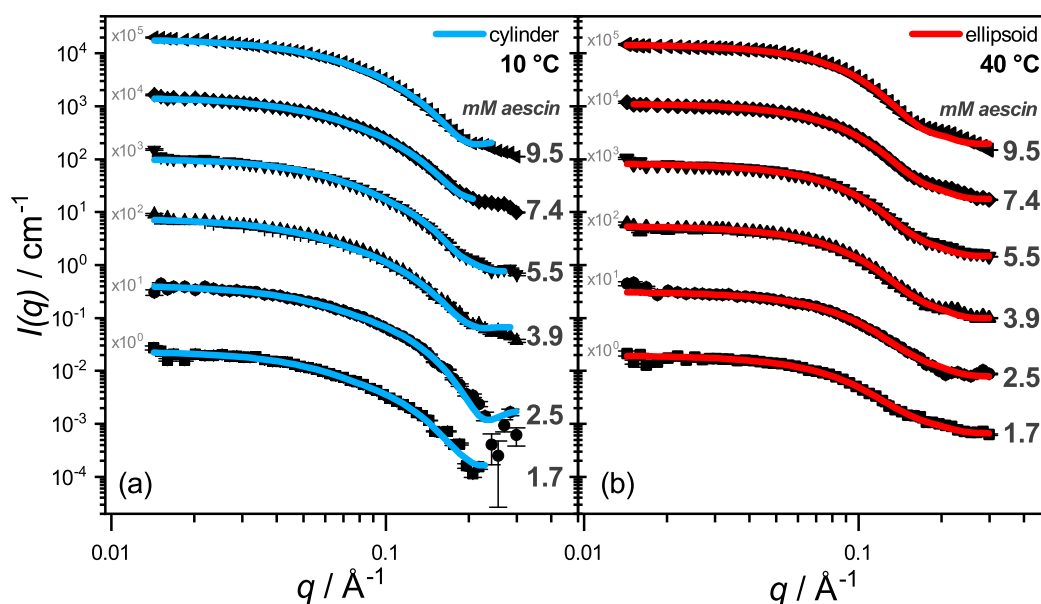


Figure 7. Model fits to the SAXS data at (a) 10 and (b) 40 °C. Data at 10 °C were fitted with a *cylinder* model and at 40 °C with an *ellipsoid* model. Both models are implemented in SASView [58]. The data are scaled by the factors given in gray.

The models follow the data for all concentrations with good agreement. This validates the structural picture introduced by TEM at low temperature and the one derived from the $p(r)$ functions for both temperatures. The cylinder model contains a radius R , a length L with polydispersity $\sigma(L)$. For the ellipsoid the fit parameters are the polar radius R_p and the equatorial radius R_e . All fit parameters are summarized in Table 2. Moreover, other parameters such as the X-ray scattering length densities of the solvent and the aescin micelles ($\text{XSLD}_{\text{H}_2\text{O}}$ and $\text{XSLD}(\text{aescin})$) were either set constant or treated as adjustable parameters (scale & background). Whereas, the XSLDs of the solvent (H_2O) were corrected for temperature ($\text{XSLD}_{\text{H}_2\text{O}}(10\text{ °C}) = 9.47 \times 10^{-6} \text{ Å}^{-2}$ and $\text{XSLD}_{\text{H}_2\text{O}}(40\text{ °C}) = 9.40 \times 10^{-6} \text{ Å}^{-2}$), for aescin, the same value was used at both temperatures ($\text{XSLD}(\text{aescin}) = 13.4 \times 10^{-6} \text{ Å}^{-2}$). The XSLD of aescin was derived from its molar volume determined from the chemical structure with ChemsSketch [59] (see also [60]). The polydispersity of the cylinder radius $\sigma(R)$ was also fitted but remained in the range from 0–10 %. Therefore, it is not explicitly mentioned.

Table 2. Fit parameters from the *cylinder* at 10 °C and *ellipsoid* fit at 40 °C. R and L are the radius and length of the cylinder. $\sigma(L)$ is the polydispersity of L . R_e and R_p are the equatorial and the polar radius of the ellipsoid, respectively.

c_{aescin} mM	R Å	L Å	$\sigma(L)$ %	R_p Å	R_e Å
1.7	17.8 ± 0.02	90.9 ± 0.4	4	13.2 ± 0.10	31.9 ± 0.07
2.5	16.8 ± 0.04	90.9 ± 0.4	14	13.4 ± 0.10	31.1 ± 0.07
3.9	17.4 ± 0.03	86.6 ± 0.2	23	15.0 ± 0.04	31.1 ± 0.05
5.5	17.8 ± 0.01	77.9 ± 0.2	26	15.4 ± 0.06	31.2 ± 0.04
7.4	18.5 ± 0.02	76.3 ± 0.2	27	15.7 ± 0.04	31.1 ± 0.03
9.5	18.5 ± 0.01	74.0 ± 0.0	26	16.8 ± 0.02	30.8 ± 0.02

The comparison of the fit results of the cylinder model at 10 °C shows that the sample concentration has a rather small impact on the diameters of the rods ($2 \cdot R$). These values remain nearly constant and are in very good agreement with the TEM results and the results from the $p(r)$ functions. Similar dimensions were reported by Matsuoka et al. [21] for the saponin glycyrrhizic acid. Depending on pH they reported values between 13 and 15 Å for the radius and 180 and 210 Å for the length of the rods. In the present case, the radii are slightly larger which may be due to the supplementary sugar group in the aescin molecule. In addition, we observe an apparent decrease of the rod-length L with increasing aescin concentration. However, the errors of L given in Table 2 result from the fitting routine and are most likely an underestimation. Moreover, the rod-length polydispersity $\sigma(L)$ also increases drastically. Hence, we think that this change of L might not be significant. At high temperature, the cylinder structure is disrupted and a higher curvature between aescin molecules is induced. In that case, the equatorial radius R_e remains constant whereas the polar radius R_p increases slightly with increasing aescin concentration. Herewith, the micelles tend to become more spherical with increasing concentration. However, the mechanism for the formation of rod-like micelles at low temperature and more spherical ones at higher temperature in viewpoints of molecular interactions cannot be resolved in this work. It should be addressed in the future using MD simulations. Moreover, the peculiar structure of aescin micelles cannot simply be estimated by the packing parameter. The complex molecular structure of aescin (e.g., hydrophilic groups attached to the backbone) differs from the 'typical' one defined by Israelachvili [61,62] which only takes one fully hydrophilic headgroup and one fully hydrophobic portion into account.

4. Conclusions and Outlook

In this work, the critical micelle concentration of aescin was determined at constant pH of 7.4 from the concentration-dependent autofluorescence of aescin in a temperature-dependent manner. Values between $cmc_{\text{aescin,AF}}(10^\circ\text{C}) = 0.38 \pm 0.09$ mM and $cmc_{\text{aescin,AF}}(50^\circ\text{C}) = 0.32 \pm 0.13$ mM were obtained. Hence, a temperature dependency of $cmc_{\text{aescin,AF}}$ was not observed within the experimental error. The autofluorescence method was verified by additional tensiometry measurements. From this method, a value of $cmc_{\text{aescin,T(WP)}}(23^\circ\text{C}) = 0.33 \pm 0.02$ mM is determined. Values obtained by both methods at similar temperatures are identical, which confirms the significance of the autofluorescence method.

Additionally, the structure of aescin micelles was investigated in a concentration-dependent manner by small-angle X-ray scattering. The investigation was done at two temperatures. At low temperature (10 °C), the micelles exhibit a rod-like structure with an average R_G of ≈ 31 Å. The shape and size of these micelles at low temperature was further confirmed by transmission electron microscopy. At high temperature, the micelles are found to be more symmetric exhibiting ellipsoidal shape. The average R_G is ≈ 21 Å. Herewith, a significant structural change of the aescin micelles occurs with increasing temperature, which can either be based on a change of the molecular packing or a reduction of forces between adjacent aescin molecules in the micellar structures. Potential triggers influencing the manner of packing may be the formation of hydrogen bonds between the polar

groups of aescin molecules and hydration with water molecules. Both vary with temperature and therefore lead to small temperature-dependent differences in the shape of the micelles formed during self-assembly. The *cmc* of aescin seems to be unaffected by the different micelle shapes formed at different temperatures. The exact mechanism for the aescin micelle formation should be addressed in a separate MD simulation study.

Supplementary Materials: The following are available online at <http://www.mdpi.com/2504-5377/3/2/47/s1>, Figure S1: LC-MS run of aescin fractions 1 and 2, Figure S2: Mass spectra of aescin fractions belonging to LC-MS run, Figure S3: ¹H-NMR spectra of aescin fractions, Figure S4: Assignment of protons in the aescin structure to ¹H-NMR signals, Figure S5: Titration curve of aescin in aqueous solution, Figure S6: Concentration-normalized autofluorescence of aescin, Figure S7: Surface tension isotherm obtained by the Du Noüy ring method, Figure S8: Time-dependent SFT measurement at constant aescin concentration, Table S1: List of ¹H-NMR signals.

Author Contributions: Conceptualization, C.D., R.G., and T.H.; Investigation, C.D., R.G., Y.H., and I.K.; Visualization, C.D. and R.G.; Writing and editing, C.D., R.G., and T.H.; Supervision, N.S. and T.H.

Funding: This research was funded by Deutsche Forschungsgemeinschaft (DFG) grant numbers HE2995/7-1, INST 215/432-1 FUGG, INST 215/444-1. We acknowledge support for the Article Processing Charge by the Deutsche Forschungsgemeinschaft and the Open Access Publication Fund of Bielefeld University.

Acknowledgments: This work benefited from the use of the SasView application, originally developed under NSF award DMR-0520547. SasView contains code developed with funding from the European Union's Horizon 2020 research and innovation program under the SINE2020 project, grant agreement No. 654000.

Conflicts of Interest: The authors declare no conflict of interest.

References

1. Watzl, B. Saponine: Charakteristik, Vorkommen, Aufnahme, Stoffwechsel, Wirkungen. *Ernährungs-Umschau* **2001**, *48*, 251–253.
2. Francis, G.; Kerem, Z.; Makkar, H.P.S.; Becker, K. The biological action of saponins in animal systems: A review. *Br. J. Nutr.* **2002**, *88*, 587–605. [[CrossRef](#)] [[PubMed](#)]
3. Güçlü-Üstündağ, Ö.; Mazza, G. Saponins: Properties, applications and processing. *Crit. Rev. Food Sci. Nutr.* **2007**, *47*, 231–258. [[CrossRef](#)] [[PubMed](#)]
4. Golemanov, K.; Tcholakova, S.; Denkov, N.; Pelan, E.; Stoyanov, S.D. Remarkably high surface visco-elasticity of adsorption layers of triterpenoid saponins. *Soft Matter* **2013**, *9*, 5738–5752. [[CrossRef](#)]
5. Vincken, J.P.; Heng, L.; de Groot, A.; Gruppen, H. Saponins, classification and occurrence in the plant kingdom. *Phytochemistry* **2007**, *68*, 275–297. [[CrossRef](#)] [[PubMed](#)]
6. Hostettmann, K.; Marston, A. *Saponins*; Cambridge University Press: Cambridge, UK; New York, NY, USA, 1995.
7. Sparg, S.G.; Light, M.E.; van Staden, J. Biological activities and distribution of plant saponins. *J. Ethnopharmacol.* **2004**, *94*, 219–243. [[CrossRef](#)]
8. Cheok, C.Y.; Salman, H.A.K.; Sulaiman, R. Extraction and quantification of saponins: A review. *Food Res. Int.* **2014**, *59*, 16–40. [[CrossRef](#)]
9. Sirtori, C.R. Aescin: Pharmacology, pharmacokinetics and therapeutic profile. *Pharmacol. Res.* **2001**, *44*, 183–193. [[CrossRef](#)]
10. Vasiliauskas, A.; Leonavičienė, L.; Vaitkienė, D.; Bradūnaitė, R.; Lukšienė, A. Anti-inflammatory effects of *Aesculus hippocastanum* L. tincture and the pro-/antioxidant bodily state of rats with adjuvant arthritis. *Acta Med. Litu.* **2010**, *17*, 123–132. [[CrossRef](#)]
11. Miyakoshi, M.; Tamura, Y.; Masuda, H.; Mizutani, K.; Tanaka, O.; Ikeda, T.; Ohtani, K.; Kasai, R.; Yamasaki, K. Antiyeast Steroidal Saponins from *Yucca schidigera* (Mohave Yucca), a New Anti-Food-Deteriorating Agent. *J. Nat. Prod.* **2000**, *63*, 332–338. [[CrossRef](#)]
12. Anisimov, M.M.; Shentsova, E.B.; Shcheglov, V.V.; Shumilov, Y.N.; Rasskazov, V.A.; Strigina, L.I.; Chetyrina, N.S.; Elyakov, G.B. Mechanism of cytotoxic action of some triterpene glycosides. *Toxicol* **1978**, *16*, 207–218. [[CrossRef](#)]
13. Gauthier, C.; Legault, J.; Girard-Lalancette, K.; Mshvildadze, V.; Pichette, A. Haemolytic activity, cytotoxicity and membrane cell permeabilization of semi-synthetic and natural lupane- and oleanane-type saponins. *Bioorg. Med. Chem.* **2009**, *17*, 2002–2008. [[CrossRef](#)] [[PubMed](#)]

14. Fukuda, K.; Utsumi, H.; Shoji, J.; Hamada, A. Saponins can cause the agglutination of phospholipid vesicles. *Biochim. Biophys. Acta Biomembr.* **1985**, *820*, 199–206. [[CrossRef](#)]
15. Lorent, J.H.; Quetin-Leclercq, J.; Mingeot-Leclercq, M.P. The amphiphilic nature of saponins and their effects on artificial and biological membranes and potential consequences for red blood and cancer cells. *Org. Biomol. Chem.* **2014**, *12*, 8803–8822. [[CrossRef](#)] [[PubMed](#)]
16. Paepenmüller, T.; Müller-Goymann, C.C. Influence of Quil A on liposomal membranes. *Int. J. Pharm.* **2014**, *475*, 138–146. [[CrossRef](#)] [[PubMed](#)]
17. Böttcher, S.; Drusch, S. Saponins—Self-assembly and behavior at aqueous interfaces. *Adv. Colloid Interface Sci.* **2017**, *243*, 105–113. [[CrossRef](#)] [[PubMed](#)]
18. Böttger, S.; Hofmann, K.; Melzig, M.F. Saponins can perturb biologic membranes and reduce the surface tension of aqueous solutions: A correlation? *Bioorg. Med. Chem.* **2012**, *20*, 2822–2828. [[CrossRef](#)] [[PubMed](#)]
19. Balakrishnan, S.; Varughese, S.; Deshpande, A. Micellar characterisation of saponin from *Sapindus mukorossi*. *Tenside Surfactants Deterg.* **2006**, *43*, 262–268. [[CrossRef](#)]
20. Liu, J.; Harms, M.; Garamus, V.M.; Müller-Goymann, C.C. Reentrant structural phase transition in amphiphilic self-assembly. *Soft Matter* **2013**, *9*, 6371. [[CrossRef](#)]
21. Matsuoka, K.; Miyajima, R.; Ishida, Y.; Karasawa, S.; Yoshimura, T. Aggregate formation of glycyrrhizic acid. *Colloids Surf. A Physicochem. Eng. Asp.* **2016**, *500*, 112–117. [[CrossRef](#)]
22. Pedebos, C.; Pol-Fachin, L.; Pons, R.; Teixeira, C.V.; Verli, H. Atomic model and micelle dynamics of QS-21 saponin. *Molecules* **2014**, *19*, 3744–3760. [[CrossRef](#)] [[PubMed](#)]
23. Peixoto, M.P.G.; Treter, J.; de Resende, P.E.; da Silveira, N.P.; Ortega, G.G.; Lawrence, M.J.; Dreiss, C.A. Wormlike micellar aggregates of saponins from *Ilex paraguariensis* A. St. Hil. (mate): A characterisation by cryo-TEM, rheology, light scattering and small-angle neutron scattering. *J. Pharm. Sci.* **2011**, *100*, 536–546. [[CrossRef](#)]
24. Demana, P.H.; Davies, N.M.; Vosgerau, U.; Rades, T. Pseudo-ternary phase diagrams of aqueous mixtures of Quil A, cholesterol and phospholipid prepared by the lipid-film hydration method. *Int. J. Pharm.* **2004**, *270*, 229–239. [[CrossRef](#)] [[PubMed](#)]
25. Dai, X.; Shi, X.; Yin, Q.; Ding, H.; Qiao, Y. Multiscale study on the interaction mechanism between ginsenoside biosurfactant and saikosaponin A. *J. Colloid Interface Sci.* **2013**, *396*, 165–172. [[CrossRef](#)] [[PubMed](#)]
26. Dreiss, C.A.; Feng, Y. *Wormlike Micelles*; Royal Society of Chemistry: Cambridge, UK, 2017.
27. Wang, Y.G.; Dai, X.X.; Shi, X.Y.; Qiao, Y.J. The simulation on self-aggregated glycyrrhizin structures. *Int. J. Appl. Math. Stat.* **2013**, *50*, 272–279.
28. Wang, Y.; Zhao, B.; Wang, S.; Liang, Q.; Cai, Y.; Yang, F.; Li, G. Formulation and evaluation of novel glycyrrhizic acid micelles for transdermal delivery of podophyllotoxin. *Drug Deliv.* **2016**, *23*, 1623–1635. [[CrossRef](#)] [[PubMed](#)]
29. Costantini, A. Escin in pharmaceutical oral dosage forms: Quantitative densitometric HPTLC determination. *Il Farmaco* **1999**, *54*, 728–732. [[CrossRef](#)]
30. Golemanov, K.; Tcholakova, S.; Denkov, N.; Pelan, E.; Stoyanov, S.D. The role of the hydrophobic phase in the unique rheological properties of saponin adsorption layers. *Soft Matter* **2014**, *10*, 7034–7044. [[CrossRef](#)] [[PubMed](#)]
31. Wilkinson, J.A.; Brown, A.M.G. Horse chestnut *aesculus hippocastanum*: Potential applications in cosmetic skin-care products. *Int. J. Cosmet. Sci.* **1999**, *21*, 437–447. [[CrossRef](#)] [[PubMed](#)]
32. Sipos, W.; Reutterer, B.; Frank, M.; Unger, H.; Grassauer, A.; Prieschl-Grassauer, E.; Doerfler, P. Escin inhibits type I allergic dermatitis in a novel porcine model. *Int. Arch. Allergy Immunol.* **2013**, *161*, 44–52. [[CrossRef](#)]
33. Zhou, X.Y.; Fu, F.H.; Li, Z.; Dong, Q.J.; He, J.; Wang, C.H. Escin, a natural mixture of triterpene saponins, exhibits antitumor activity against hepatocellular carcinoma. *Planta Medica* **2009**, *75*, 1580–1585. [[CrossRef](#)] [[PubMed](#)]
34. Dudek-Makuch, M.; Studzińska-Sroka, E. Horse chestnut—Efficacy and safety in chronic venous insufficiency: An overview. *Rev. Bras. Farmacogn.* **2015**, *25*, 533–541. [[CrossRef](#)]
35. Khan, L.; Kifayatullah, Q.; Ahmad, K.D.; Arfan, M. Preparation of water-soluble aescin from *aesculus-indica* seeds. *J. Chem. Soc. Pak.* **1994**, *16*, 269–272.
36. Wulff, G.; Tschesche, R. Über Triterpene-XXVI: Über die Struktur der Roskastaniensaponie (Aescin) und die aglykone verwandter Glykoside. *Tetrahedron* **1969**, *25*, 415–436. [[CrossRef](#)]

37. Pittler, M.H.; Ernst, E. Horse-Chestnut Seed Extract for Chronic Venous Insufficiency. *Arch. Dermatol.* **1998**, *134*, 1356–1360. [[CrossRef](#)] [[PubMed](#)]
38. Arnould, T.; Janssens, D.; Michiels, C.; Remacle, J. Effect of aescine on hypoxia-induced activation of human endothelial cells. *Eur. J. Pharmacol.* **1996**, *315*, 227–233. [[CrossRef](#)]
39. Sreij, R.; Dargel, C.; Geisler, P.; Hertle, Y.; Radulescu, A.; Pasini, S.; Perez, J.; Moleiro, L.H.; Hellweg, T. DMPC vesicle structure and dynamics in the presence of low amounts of the saponin aescin. *Phys. Chem. Chem. Phys.* **2018**, *20*, 9070–9083. [[CrossRef](#)] [[PubMed](#)]
40. Sreij, R.; Dargel, C.; Hannappel, Y.; Jestin, J.; Prévost, S.; Dattani, R.; Wrede, O.; Hellweg, T. Temperature Dependent Self-Organization of DMPC Membranes Promoted by Intermediate Amounts of the Saponin Aescin. *Biochim. Biophys. Acta Biomembr.* **2019**, *1861*, 897–906. [[CrossRef](#)]
41. Sreij, R.; Dargel, C.; Moleiro, L.H.; Monroy, F.; Hellweg, T. Aescin Incorporation and Nanodomain Formation in DMPC Model Membranes. *Langmuir* **2017**, *33*, 12351–12361. [[CrossRef](#)]
42. De Groot, C.; Müsken, M.; Müller-Goymann, C.C. Novel Colloidal Microstructures of β -Escin and the Liposomal Components Cholesterol and DPPC. *Planta Medica* **2018**, *84*, 1219–1227. [[CrossRef](#)] [[PubMed](#)]
43. Penfold, J.; Thomas, R.K.; Tucker, I.; Petkov, J.T.; Stoyanov, S.D.; Denkov, N.; Golemanov, K.; Tcholakova, S.; Webster, J.R.P. Saponin Adsorption at the Air-Water Interface-Neutron Reflectivity and Surface Tension Study. *Langmuir* **2018**, *34*, 9540–9547. [[CrossRef](#)] [[PubMed](#)]
44. Pekdemir, T.; Ishigami, Y.; Uchiyama, H. Characterization of Aescin as a biosurfactant for environmental remediation. *J. Surfactants Deterg.* **1999**, *2*, 337–341. [[CrossRef](#)]
45. Yoshikawa, M.; Murakami, T.; Matsuda, H.; Yamahara, J.; Murakami, N.; Kitagawa, I. Bioactive saponins and glycosides. III. Horse chestnut.(1): The structures, inhibitory effects on ethanol absorption, and hypoglycemic activity of escins Ia, Ib, IIa, IIb, and IIIa from the seeds of *Aesculus hippocastanum* L. *Chem. Pharm. Bull.* **1996**, *44*, 1454–1464. [[CrossRef](#)] [[PubMed](#)]
46. Yoshikawa, M.; Murakami, T.; Yamahara, J.; Matsuda, H. Bioactive saponins and glycosides. XII. Horse chestnut.(2): Structures of escins IIIb, IV, V, and VI and isoescins Ia, Ib, and V, acylated polyhydroxyoleanene triterpene oligoglycosides, from the seeds of horse chestnut tree (*Aesculus hippocastanum* L., Hippocastanaceae). *Chem. Pharm. Bull.* **1998**, *46*, 1764–1769. [[PubMed](#)]
47. Zhang, F.; Ilavsky, J.; Long, G.G.; Quintana, J.P.G.; Allen, A.J.; Jemian, P.R. Glassy carbon as an absolute intensity calibration standard for small-angle scattering. *Metall. Mater. Trans. A* **2010**, *41A*, 1151–1158. [[CrossRef](#)]
48. Viguiet, G.; Girardot, R.; Perez, J. Foxtrot 3.3.4. 2016.
49. Nakahara, Y.; Kida, T.; Nakatsuji, Y.; Akashi, M. New fluorescence method for the determination of the critical micelle concentration by photosensitive monoazacryptand derivatives. *Langmuir* **2005**, *21*, 6688–6695. [[CrossRef](#)] [[PubMed](#)]
50. Abuin, E.B.; Lissi, E.A.; Aspée, A.; Gonzalez, F.D.; Varas, J.M. Fluorescence of 8-Anilino-naphthalene-1-sulfonate and Properties of Sodium Dodecyl Sulfate Micelles in Water–Urea Mixtures. *J. Colloid Interface Sci.* **1997**, *186*, 332–338. [[CrossRef](#)]
51. Asakawa, T.; Mouri, M.; Miyagishi, S.; Nishida, M. Probe methods for the second cmc of fluorocarbon and hydrocarbon surfactant mixtures. *Langmuir* **1989**, *5*, 343–348. [[CrossRef](#)]
52. Tsibranska, S.R.; Ivanova, A.; Tcholakova, S.; Denkov, N.D. Self-Assembly of Escin Molecules at the Air-Water Interface as Studied by Molecular Dynamics. *Langmuir* **2017**, *33*, 8330–8341. [[CrossRef](#)]
53. El-Hefian, E.A.; Yahaya, A.H. Investigation on Some Properties of SDS Solutions. *Aust. J. Basic Appl. Sci.* **2011**, *5*, 1221–1227.
54. Janek, T.; Czyżnikowska, Ż.; Łuczyński, J.; Gudiña, E.J.; Rodrigues, L.R.; Gałęzowska, J. Physicochemical study of biomolecular interactions between lysosomotropic surfactants and bovine serum albumin. *Colloids Surf. B Biointerfaces* **2017**, *159*, 750–758. [[CrossRef](#)] [[PubMed](#)]
55. Milanović, M.; Krstonošić, V.; Dokić, L.; Hadnađev, M.; Dapčević Hadnađev, T. Insight into the interaction between carbopol® 940 and ionic/nonionic surfactant. *J. Surfactants Deterg.* **2015**, *18*, 505–516. [[CrossRef](#)]
56. Stanimirova, R.; Marinova, K.; Tcholakova, S.; Denkov, N.; Stoyanov, S.; Pelan, E. Surface rheology of saponin adsorption layers. *Langmuir* **2011**, *27*, 12486–12498. [[CrossRef](#)] [[PubMed](#)]
57. Bergmann, A.; Fritz, G.; Glatter, O. Solving the generalized indirect Fourier transformation (GIFT) by Boltzmann simplex simulated annealing (BSSA). *J. Appl. Crystallogr.* **2000**, *33*, 1212–1216. [[CrossRef](#)]

58. SASView, Freeware Version 4.20 beta. 2018. Available online: <http://www.sasview.org> (accessed on 20 July 2018).
59. ACD/ChemSketch, Freeware Version; Advanced Chemistry Development, Inc.: Toronto, ON, Canada, 2015. Available online: <http://www.acdlabs.com> (accessed on 12 March 2018).
60. Sreij, R.; Prévost, S.; Dattani, R.; Dargel, C.; Hertle, Y.; Wrede, O.; Hellweg, T. Interaction of the saponin aescin with ibuprofen in DMPC model membranes. *Mol. Pharm.* **2018**, *15*, 4446–4461. [[CrossRef](#)] [[PubMed](#)]
61. Israelachvili, J.N. *Thermodynamic and Geometric Aspects of Amphiphile Aggregation into Micelles, Vesicles and Bilayers, and the Interactions between Them*; North-Holland: Amsterdam, The Netherlands, 1985; pp. 24–58.
62. Israelachvili, J.N. *Intermolecular and Surface Forces*, 2nd ed.; Academic Press: New York, NY, USA, 1992.



© 2019 by the authors. Licensee MDPI, Basel, Switzerland. This article is an open access article distributed under the terms and conditions of the Creative Commons Attribution (CC BY) license (<http://creativecommons.org/licenses/by/4.0/>).